Materials Today Energy 37 (2023) 101383

Contents lists available at ScienceDirect

Materials Today Energy

journal homepage: www.journals.elsevier.com/materials-today-energy/

Stretchable polyvinyl alcohol and sodium alginate double network ionic hydrogels for low-grade heat harvesting with ultrahigh thermopower

Yi-Chun Hsiao [a, e], Ling-Chieh Lee [a, e], Yen-Ting Lin [a], Shao-Huan Hong [b], Kuan-Chieh Wang [a], Shih-Huang Tung [c], Cheng-Liang Liu [a, d, *]

[a] Department of Materials Science and Engineering, National Taiwan University, Taipei, 10617, Taiwan
[b] Department of Chemical and Materials Engineering, National Central University, Taoyuan, 32001, Taiwan
[c] Institute of Polymer Science and Engineering, National Taiwan University, Taipei, 10617, Taiwan
[d] Advanced Research Center for Green Materials Science and Technology, National Taiwan University, Taipei, 10617, Taiwan

ARTICLE INFO

Article history:
Received 27 July 2023
Received in revised form
9 August 2023
Accepted 10 August 2023
Available online 15 August 2023

Keywords:
Ionic thermoelectric
Hydrogel
Poly (vinyl alcohol)
Seebeck coefficient

ABSTRACT

Recently, employing ionic thermoelectric (i-TE) materials is regarded as a promising strategy to harness low-grade waste heat due to their remarkable ionic Seebeck coefficient. By blending polyvinyl alcohol (PVA), sodium alginate (SA), and polyethylene glycol (PEG) and additional freeze-thaw method, PVA/SA/PEG hydrogel is developed. Via immersing the hydrogel in $NaBF_4$ solutions with different concentrations, the TE and mechanical properties could be adjusted. PVA/SA/PEG/$NaBF_4$-1.5 M hydrogel demonstrates exceptional mechanical properties, with tensile stress and strain up to 69 kPa and 114%, respectively. Moreover, PVA/SA/PEG/$NaBF_4$-1.5 M hydrogel exhibits a high ionic conductivity of 31.4 mS/cm, a maximum ionic Seebeck coefficient of 66.7 mV/K, and an impressive power factor of 13.96 mW/m/K^2. These outstanding performances originate from the synergistic effect of Manning's counterion condensation facilitated by SA and the crystal PVA chains. The prototype application of the PVA/SA/PEG/$NaBF_4$-1.5 M hydrogel is demonstrated by a flexible ionic thermoelectric supercapacitor. With the external load resistance is 90 kΩ, the energy collected in one thermal cycle could achieve 4 mJ. This study introduces the exceptional stretchable PVA/SA/PEG/$NaBF_4$ hydrogels with a record-high ionic Seebeck coefficient as promising i-TE materials for future TE application in low-grade waste heat.

© 2023 Elsevier Ltd. All rights reserved.

1. Introduction

As industries have experienced significant growth and development, there has been a notable improvement in the quality of human life. However, the reliance on traditional fossil fuel-based energy sources has resulted in numerous environmental challenges and energy crises [1]. The emission of greenhouse gases from these sources has led to severe air pollution and climate issues. Consequently, researchers are now actively working towards developing energy-harvesting techniques from waste heat to achieve environmental sustainability. Waste heat typically exists in the form of low-grade heat with temperatures below 100 °C. It is available in various settings, such as daily environments, industrial production processes, and waste heat generated by the human body. Previous studies have explored methods for converting low-grade heat into electricity, including Organic Rankine Cycles (ORCs) [2], Kalina cycles [3], inverted Brayton cycles [4], and thermoelectric (TE) conversion [5]. Among these, the first three methods have not been extensively adopted for low-grade thermal energy conversion due to their low energy conversion efficiency and system complexity. However, TE conversion has emerged as a key player in the recovery of waste heat energy from sources such as solar radiation, industrial processes, and biological heat. When a thermal gradient (ΔT) is applied to a TE material, such that one side is exposed to heat (T_H) while the other side remains cold (T_c), this creates a voltage gradient (ΔV), where $\Delta V = V_H - V_C$, which, in turn, generates an electrical current via the diffusion of charge carriers (electrons or holes) [6–8]. This is known as the Seebeck effect, and its strength is measured by the Seebeck coefficient (S). In addition,

* Corresponding author.
E-mail address: liucl@ntu.edu.tw (C.-L. Liu).
[e] These authors contributed equally to this work.

https://doi.org/10.1016/j.mtener.2023.101383
2468-6069/© 2023 Elsevier Ltd. All rights reserved.

when TE materials are employed in thermoelectric generators (TEGs), the thermal conductivity (κ, in W/m/K) should be minimized to maintain the ΔV between the hot and cold sides, and a higher electrical conductivity (σ_e) is desirable to reduce energy losses due to Joule heating. The TE properties of a material are evaluated using the dimensionless figure of merit (ZT), $ZT = \sigma S^2 T \kappa^{-1}$, which is dependent on the absolute temperature, the electrical transport properties (i.e., power factor, $PF = S_i^2\sigma_i$) and the thermal conductance of the materials. In addition, because the thermal conductivities of polymer-based TE materials are relatively low and similar (around 0.1–0.5 W/m/K), increasing PF of materials is the main target for ZT value enhancement since organic materials generally have intrinsic low thermal conductivity (around 0.1–0.5 W/m/K). Meanwhile, enhancing the Seebeck coefficient is crucial for improving the TE properties, as it is a squared term in both the ZT and PF values [9,10]. Hence, by further optimizing the composition and structure of a TE material, its TE performance can be improved but achieving efficient TEGs poses significant challenges due to the strong coupling between electrical conductivity, Seebeck coefficient, and thermal conductivity [11,12].

Inorganic semiconductors are widely used as electron-based thermoelectric (e-TE) materials [13–19]. However, their applications are limited by their low Seebeck coefficients of around a hundred μV/K. Additionally, these materials often contain rare elements, lack mechanical flexibility, and pose challenges in terms of toxicity and cost. By contrast, ionic thermoelectric (i-TE) materials, use the movement of ions as energy carriers through the electrolyte, thereby affording one to three orders of magnitude larger Seebeck coefficient (termed the ionic Seebeck coefficient, S_i) than that of the e-TE materials. The i-TE material devices are typically sub-categorized as thermogalvanic cells (TGCs) and thermally chargeable capacitors (TCCs) and both can be prepared in liquid or quasi-soild base [20–23] which are commonly composed of inexpensive, abundant, and environmentally friendly materials such as water and polymers. Moreover, the use of polymer as i-TE materials enhances their practical potential by providing high stretchability [24] and flexibility, thus making them suitable for use in wearable devices for Internet of Things (IoT) and other societal applications [25–32].

When compared to the TGCs, which operate on the basis of Faraday redox reactions near the electrodes [33], the TCCs can generate ionic Seebeck coefficients of dozens of mV/K via the Soret effect, which relies on the thermal diffusion of ions rather than electrons or holes. Previous work on i-TE materials has mainly focused on aqueous solutions of acids or bases [34]. However, these liquid electrolytes have problems such as easy leakage, volatility, inadequate mechanical properties, lower ionic Seebeck coefficient and complicated encapsulation. Recent studies indicate that introducing a polymer matrix into a TCC system can enhance the ionic Seebeck coefficient by leveraging the interactions between the polar groups of the polymer and the ions [35,36]. Therefore, recent research, as summarized in Table S1, has focused on developing quasi-solid ionogels that confine anions and cations within polymer networks. These emerging materials have shown promise as heat harvesting materials, offering excellent mechanical strength, solving leakage problems and excellent TE properties [34,37–46]. For example, through the dipole moment interaction between poly (vinylidene fluoride-co-hexafluoropropylene) (PVDF-HFP) and an ionic liquid 1-ethyl-3-methyl-imidazolium-dicyanamide (EMIM-DCA), the resulting ionogel TCC can achieve an ionic Seebeck coefficient of 26.1 mV/K [39]. Poly (vinyl alcohol)-based hydrogel also exhibit excellent TE properties due to polymer segment provides ion selectivity [38,47]. Similarly, immersing an NaCl salt solution in a dual double network polyacrylamide/sodium carboxymethyl cellulose (PMSC) gel has resulted in an ionic Seebeck coefficient of 17.1 mV/K [46]. Such PMSC gels not only allow selective tuning of the interaction with NaCl salt, but also provide good stretchability. However, previous studies have mainly focused on a single polymer system with polar functional groups [36,39], and there remains a lack of strategies for combining two different polymer matrices in order to further enhance the ionic Seebeck coefficient.

In the present work, two types of polymer matrix are combined with the aim of improving the TE properties of the material. The double network hydrogel matrix is formed by combining polyvinyl alcohol (PVA), sodium alginate (SA), and polyethylene glycol (PEG) as a crosslinker (chemical structure as depicted in Fig. 1a) This particular matrix exhibits exceptional mechanical characteristics, with a tensile stress of 69 kPa and a strain of 114%. These properties enable the hydrogel to achieve wearable device stretchability at a tensile strain of 15% [24]. The inclusion of $NaBF_4$ further improves the ionic conductivity, which reaches a value of 31.4 mS/cm. According to the synergistic effect of Manning's counterion condensation theory [48] and crystallization behavior of PVA, an ultrahigh ionic Seebeck coefficient of 66.8 mV/K is achieved. With the advantages of low cost, ease of preparation, and excellent mechanical properties, making PVA/SA/PEG/$NaBF_4$ hydrogel a potential material for wearable devices application.

2. Experimental section

2.1. Materials

Polyvinyl alcohol (PVA) with molecular weight of 89,000–98,000 g/mol and a hydrolysis degree of 99+% hydrolyzed was procured from Sigma Aldrich. Sodium alginate (SA), and sodium tetrafluoroborate (reagent grade, 98%) were also obtained from Sigma Aldrich. The polyethylene glycol (PEG) utilized in the experiments had a molecular weight range of 380–420 g/mol and was supplied by Showa Chemicals Co., LTD. Throughout the experiments, deionized water was used as the solvent.

2.2. Preparation of PVA/SA/PEG hydrogel

The process for preparing PVA/SA/PEG hydrogels is illustrated in Fig. S1. Firstly, 2.0 g of PVA was dissolved in 20 ml of deionized water and stirred at 90 °C until complete dissolution of all solids. Next, SA was added to the solution under the same conditions, resulting in a transparent solution. Subsequently, 2.8 g of PEG was introduced as a crosslinking agent. The prepared mixture was subsequently poured into specialized molds and transferred to a refrigerator set at a temperature of −20 °C for a duration of 12 h. Following this, the molds were allowed to thaw at room temperature for a period of 6 h. This process yielded the pristine PVA/SA/PEG hydrogel, which was then carefully cut to dimensions suitable for the study, with a length of 1.5 cm, width of 1.5 cm, and height of 1 cm.

To obtain the PVA/SA/PEG/$NaBF_4$ hydrogel, the pristine PVA/SA/PEG hydrogel was immersed in solutions of different $NaBF_4$ concentrations (0.5 M, 1.0 M, 1.5 M, 2.0 M) for 1 h. The resulting hydrogels, with varying $NaBF_4$ concentrations, were denoted as PVA/SA/PEG/$NaBF_4$-0.5 M, 1.0 M, 1.5 M, 2.0 M, respectively.

2.3. Structural characterizations

The morphologies of hydrogels were examined using Hitachi S-4800 scanning electron microscope (SEM). To determine the elemental composition, energy-dispersive X-ray spectroscopy

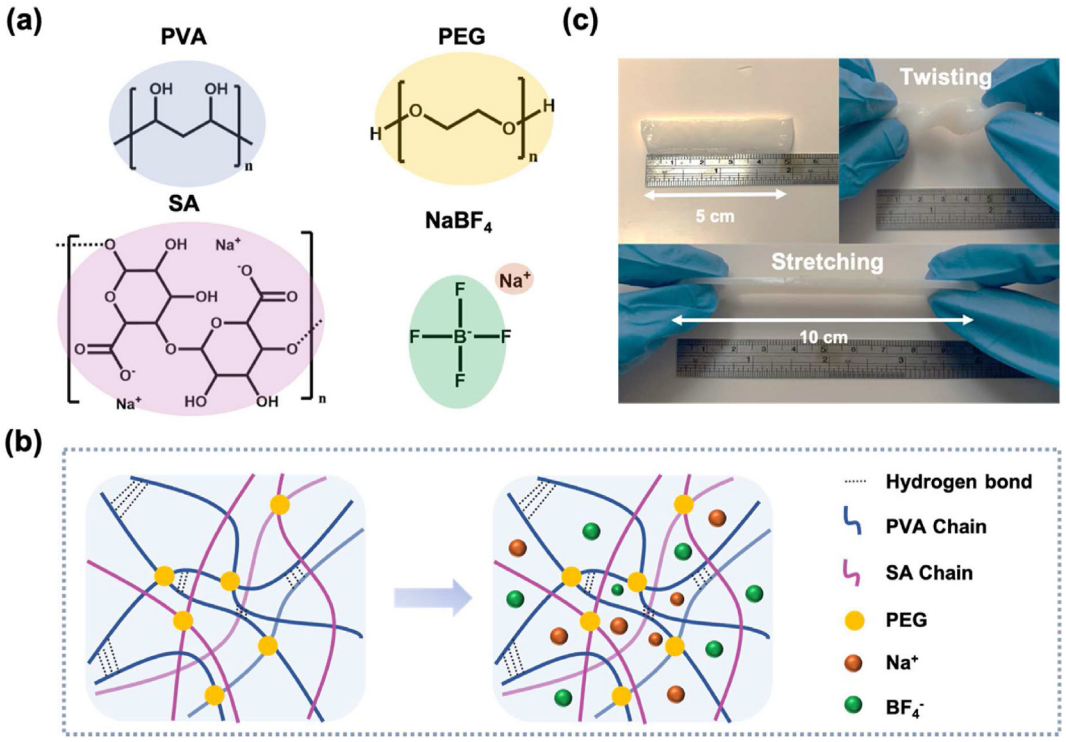

Fig. 1. (a) Chemical structures of the components used to synthesize the hydrogel: PVA, SA, PEG and $NaBF_4$. (b) Schematic representation of $NaBF_4$ electrolyte-containing hydrogel. (c) Photographs showing PVA/SA/PEG hydrogel under different conditions: initial, twisting, and stretching.

(EDS) was performed using a QUANTAX Annular XFlash® QUAD FQ5060 instrument. Fourier Transform Infrared Spectroscopy (FTIR) spectra were recorded using a PerkinElmer Spectrum TWO FT-IR L16000 spectrometer. The crystallization behavior of PVA was analyzed using X-ray diffraction (XRD) measurement conducted on a Rigaku MiniFlex instrument, covering 2θ range of 2~90°. The mechanical properties of the hydrogels were evaluated using a universal testing machine (SHIMADZU EZ-Test) on dumbshell-shaped samples with dimensions of 15 mm wide, 40 mm long, and about 5 mm thickness. The samples were subjected to tension at a speed of 2 mm/min. The rheological behavior of hydrogels was tested using a Dynamic Rheological Test on a HR-2 system (stress control). The test involved heating the hydrogels from 25 to 50 °C at a rate of 3 °C/min.

2.4. Properties measurement

The ionic conductivity was measured using BioLogic SP-50e workstation. AC impedance spectroscopy was applied in a frequency range from 1 to 1×10^6 Hz under ambient conditions. The value of ionic conductivity (σ_i) was calculated using the following equation: $\sigma_i = d/(A \times R)$, where A represents the cross-sectional area of the sample, R denotes the bulk resistance of PVA/SA/PEG/$NaBF_4$ hydrogels obtained from the intercept on the abscissa of the electrochemical impedance spectroscopy (EIS) diagram, and d signifies the thickness of the sample. The TE properties of the hydrogels were measured using a custom-built measurement system. A ΔT was introduced into the PVA/SA/PEG/$NaBF_4$ hydrogels using a laboratory circulation water bath system for heating and cooling. The temperature was monitored using a K-type thermocouple attached to the sample surfaces, and measurements were acquired with a Keithley DAQ 6510 multimeter. The voltage across the two platinum (Pt) electrodes on the sample was measured using a Keithley 2182A nanovoltmeter, as illustrated in Fig. S2.

3. Results and discussion

3.1. Structural characterization of hydrogels

The addition of PEG can increase the crystallinity of PVA, thus improving the mechanical properties and ion selectivity of the devices. SA is a natural polysaccharide with good biocompatibility and can provide excessive cations concentration thus enhancing ionic conductivity. The chemical structure of the PVA/SA/PEG hydrogel is presented in Fig. 1a.The PVA/SA/PEG/$NaBF_4$ hydrogel was synthesized successfully by using the freeze-thaw method, which proved to be an effective approach for promoting gelation [49]. The PVA/SA/PEG mixture has limited gelation at room temperature, using freeze-thaw method can produce that ice crystals form in the water-rich regions of the hydrogel upon freezing at approximately −20 °C, thus leading to decreased mobility of the PVA and SA polymers. This results in more compact polymer chains with increased hydrogen bonding, thereby enhancing gelation [50–52]. Upon thawing at around 25 °C, the ice crystals melt while the hydrogen bonds between the PVA and SA polymers remain intact, as observed in similar studies [49]. This process facilitates a more compact arrangement of polymer chains within the hydrogel, with increased hydrogen bonding and improved interconnectivity between the PVA and SA components. Further, as demonstrated by the schematic in Fig. 1b, the inclusion of PEG as a crosslinker in the hydrogel formulation contributes to its excellent mechanical performance. This is because the PEG forms hydrogen bonding networks individually between the SA and PVA, thereby connecting the polymer chains and providing stress dissipation zones. This results in a hydrogel with remarkable toughness, as demonstrated by the photographic images of the stretched and twisted material in Fig. 1c. Here, the hydrogel exhibits good flexibility without breaking, thus making it highly suitable for use in wearable thermoelectric applications. Meanwhile, in agreement with previous

studies [38,53,54] that the inclusion of the salt in the hydrogel formulation improves the ionic conductivity, thus making the hydrogel a potential candidate for use as a thermoelectric-active material. This is attributed to dissociation of the $NaBF_4$ into ions that can freely move within the hydrogel network under a ΔT, thereby promoting the Soret effect.

The microstructures of the hydrogels are revealed by the SEM images in Fig. 2. Here, the pristine PVA/SA/PEG hydrogel consisting of the double chemical network exhibits a microporous structure characterized by interconnected polymer chains (Fig. 2a). This porous structure is expected to facilitate the formation of water channels, thereby allowing ions to penetrate through the hydrogel. Indeed, the homogeneous distribution of Na^+ ions within the PVA/SA/PEG hydrogel is confirmed by the energy-dispersive X-ray spectroscopy (EDS) results in Fig. 2b. Upon soaking the pristine hydrogel in $NaBF_4$ solution, the network structure of the PVA/SA/PEG/$NaBF_4$ hydrogel becomes more compact due to the salting out effect, thus resulting in aggregation of the polymer chains, as revealed by the SEM images in Fig. 2c–f. This phenomenon is probably due to the presence of $NaBF_4$, which disrupts the stability of the interactions between the hydrated water and polymer chains, thereby increasing the surface tension surrounding the polymer chains and interfering with the hydration between polymer chains [49]. Hence, the results in Fig. 2f indicate that as the concentration of $NaBF_4$ is increased from 0.5 to 2.0 M, the network structure of the hydrogel becomes progressively more compact, thus resulting in smaller polymer channel sizes. These findings suggest that the concentration of $NaBF_4$ plays a crucial role in determining the network structure of the hydrogel.

The Intermolecular Interactions between the PVA polymer chains and the $NaBF_4$ in the hydrogels are revealed by the Fourier transform infrared (FTIR) spectra in Fig. 3. Here, the FTIR spectra of the PVA/SA/PEG hydrogel exhibits characteristic bands at 1080 cm^{-1}, 3380 cm^{-1}, and 1644 cm^{-1} due to the C–O, O–H, and C=O vibrations, respectively (Fig. 3a). Further, as the concentration of $NaBF_4$ is increased to 2.0 M, a blue shift in the O–H stretching vibration from 3380 to 3391 cm^{-1} is observed, thus indicating a stronger stretching of the hydroxyl groups due to the salting-out effect of $NaBF_4$ [42]. Additionally, the peak at 1080 cm^{-1} corresponds to the C–O stretching vibration related to the

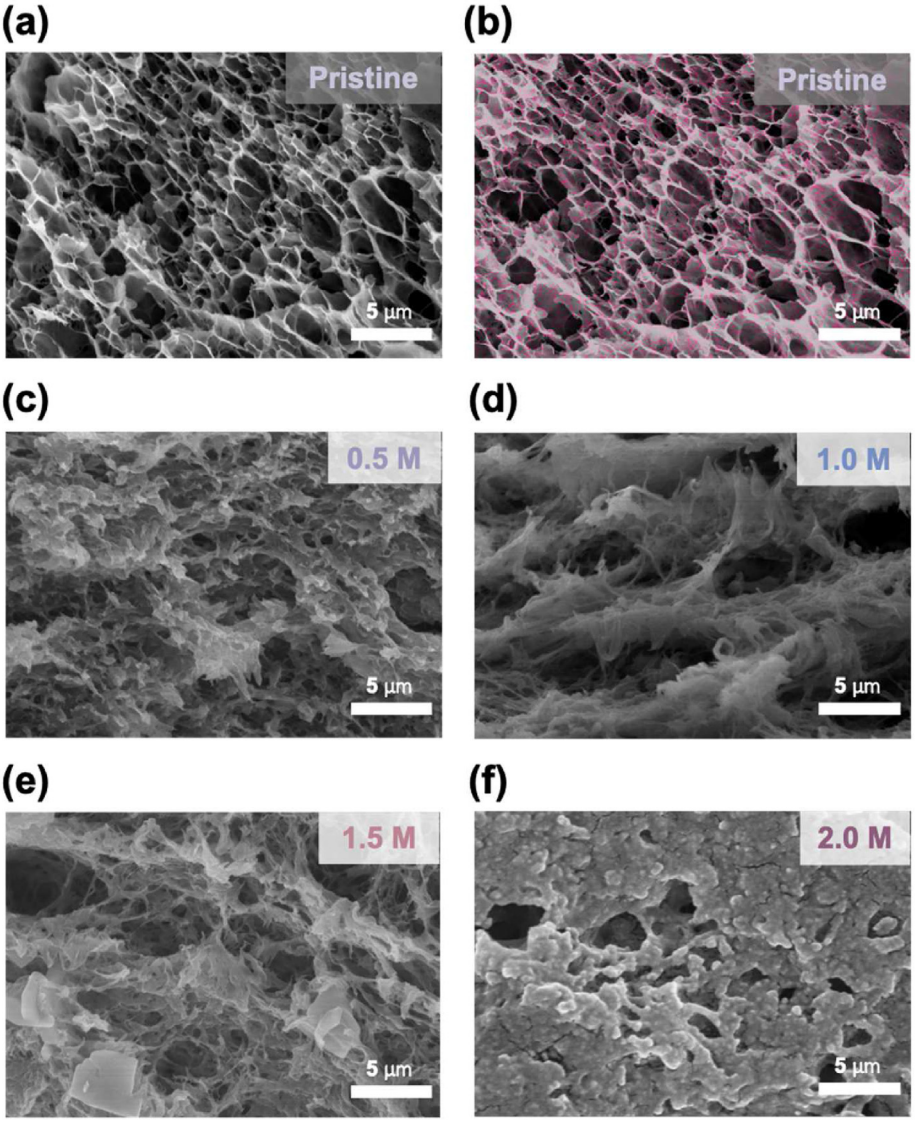

Fig. 2. (a) SEM images and (b) EDS mapping of Na element of PVA/SA/PEG DN hydrogel. SEM images of PVA/SA/PEG/$NaBF_4$ hydrogel with varying concentrations of $NaBF_4$: (c) 0.5 M, (d) 1.0 M, (e) 1.5 M, and (f) 2.0 M.

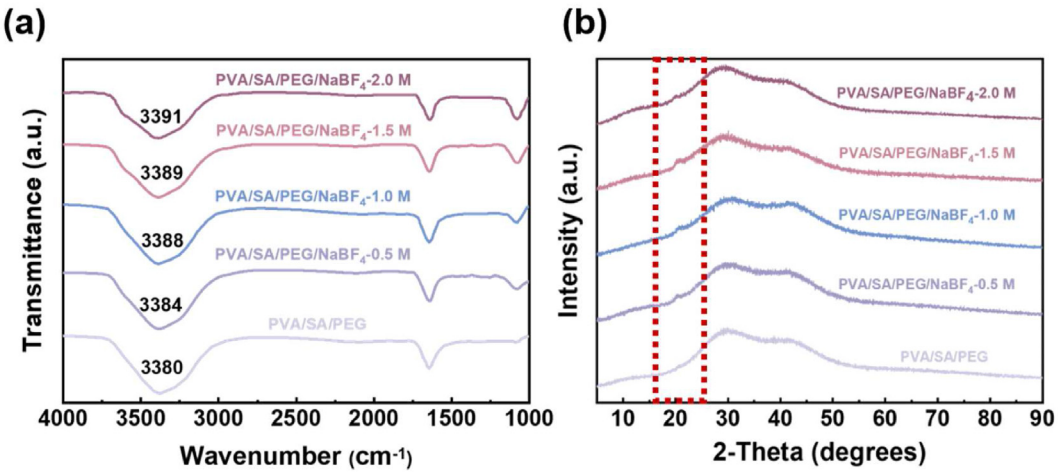

Fig. 3. (a) FTIR spectrum and (b) XRD measurement of PVA/SA/PEG/$NaBF_4$ hydrogel with varying $NaBF_4$ concentrations.

antisymmetric stretching vibration of O—C—C in PVA [38,47]. When the PVA/SA/PEG hydrogel is soaked in $NaBF_4$ solution, the intensity of the C—O peak increases due to the interactions of the ions with the polymer chains. The presence of $NaBF_4$ decreases the water content in the hydrogel, thus promoting the interactions between the PVA and SA polymer chains in the amorphous region, and leading to a peak shift in the FTIR spectrum. This is consistent with the above SEM images (Fig. 2c—f), which show increased aggregation and compactness of the network structure with increasing $NaBF_4$ concentration.

The addition of PEG has been reported to enhance the crystallinity of hydrogels, thereby resulting in increased opacity due to the interactions between polymer chains [49]. Hence, the SEM image in Fig. 2a reveals that the PVA polymer in the as-synthesized PVA/SA/PEG hydrogel exhibits a semicrystalline structure. This observation is supported by XRD results in Fig. 3b, which reveal a diffraction peak at $2\theta = 19.7^\circ$ corresponding to the $(10\bar{1})$ crystal plane of PVA [47]. Upon soaking the hydrogel in $NaBF_4$ solution, the intensity of this diffraction peak is increased, thereby indicating an increased quantity of crystalline domains in the PVA polymer chains. This finding is also in agreement with the above-mentioned FTIR spectra (Fig. 3a).

The capacity of the PVA/SA/PEG double network hydrogel matrix to undergo repeated stretching or twisting was demonstrated in Fig. 1c. The mechanical properties of the hydrogel are further revealed by the tensile measurements in Fig. 4a. Here, the PVA/SA/PEG hydrogel exhibits a lower tensile strength (~50 kPa) and a higher elongation (>140%) than those of the hydrogel that was treated with 2.0 M $NaBF_4$ (i.e., 450 kPa and 98%, respectively). This is evidenced by the increased quantity of crystalline regions in the PVA polymer chains imaged in Fig. 3b, which promote hydrogen bonding between the amorphous PVA chains, thereby resulting in a stronger network structure and improved mechanical properties. Moreover, the trend of increasing tensile strength and decreasing elongation becomes more pronounced with increasing $NaBF_4$ concentration, thus demonstrating the importance of crystallinity in determining the mechanical properties of the hydrogel.

The dynamic mechanical properties of the PVA/SA/PEG/$NaBF_4$ hydrogels in the temperature range of 20—40 °C are presented in Fig. 4b. Here, the storage modulus (G') remains consistently higher than the loss modulus (G'') for all tested concentrations of $NaBF_4$ in the hydrogels throughout the temperature range, thereby indicating that the hydrogels exhibit quasi-solid behavior rather than liquid-like behavior [55]. Moreover, the storage modulus of the PVA/SA/PEG/$NaBF_4$ hydrogel increases with increasing concentration of $NaBF_4$, which is in agreement with the observed improvement in the tensile properties. These results carry significant implications for the development of wearable thermoelectric devices, given that the hydrogel properties enable it to maintain stability even with changes in temperature.

3.2. The thermoelectric properties of the PVA/SA/PEG/$NaBF_4$ hydrogel

The ionic Seebeck coefficients of the hydrogels with $NaBF_4$ concentrations of 0—2.0 M are presented in Fig. 5a and Fig. S3, where the ionic Seebeck coefficient is obtained by fitting the $\Delta V - \Delta T$ curves. The ionic Seebeck coefficient (S_i) is generally defined as $S_i = -\frac{\Delta V}{\Delta T} = -\frac{V(T_H)-V(T_C)}{T_H-T_C}$, where V (T_H) is the voltage of the hot electrode at temperature T_H and, tand V (T_C) is that of the cold electrode at temperature T_C. When a ΔT is applied, a voltage gradient (ΔV) is produced, and this becomes more negative as ΔT increases, thereby indicating that the Na^+ cations have a higher thermal mobility than the BF_4^- anions. This, in turn, implies that the PVA/SA/PEG/$NaBF_4$ TCCs are p-type materials. Moreover, the ionic Seebeck coefficient is seen to depend on $NaBF_4$ concentration. Thus, as the concentration of $NaBF_4$ increases from 0.5 to 1.5 M (Fig. 5b and Fig. S4), the fraction of mobile cations increases, thereby resulting in a maximum ionic Seebeck coefficient of 66.7 mV/K at a concentration of 1.5 M. Notably, this is the highest value thus far reported value among TCCs (Fig. 5c) [34,37,42—44,46]. However, when the ion concentration is further increased to 2.0 M, the ionic Seebeck coefficients decreases to 7.1 mV/K. This can be attributed to the decreased ion selectivity caused by a decrease in the Debye length of the polymer. The higher ion concentration can induce a screening effect that interferes with the ability of the polymer matrix to selectively facilitate ion migration, thus resulting in reduced ion selectivity. Similar phenomena have been reported previously [40].

To understand the high ionic Seebeck coefficients observed in the PVA/SA/PEG/$NaBF_4$ hydrogels, it is important to consider the effect of ionic thermodiffusion. In i-TE materials, when a ΔT is applied, both cations and anions migrate across the electrolyte from the hot side to cold side, thus resulting in the net accumulation of charge and the generation of ΔV. This is known as the Soret effect, and involves the bipolar migration of equal numbers of anions and cations ($n^+ = n^-$). Based on the driving force of the Soret

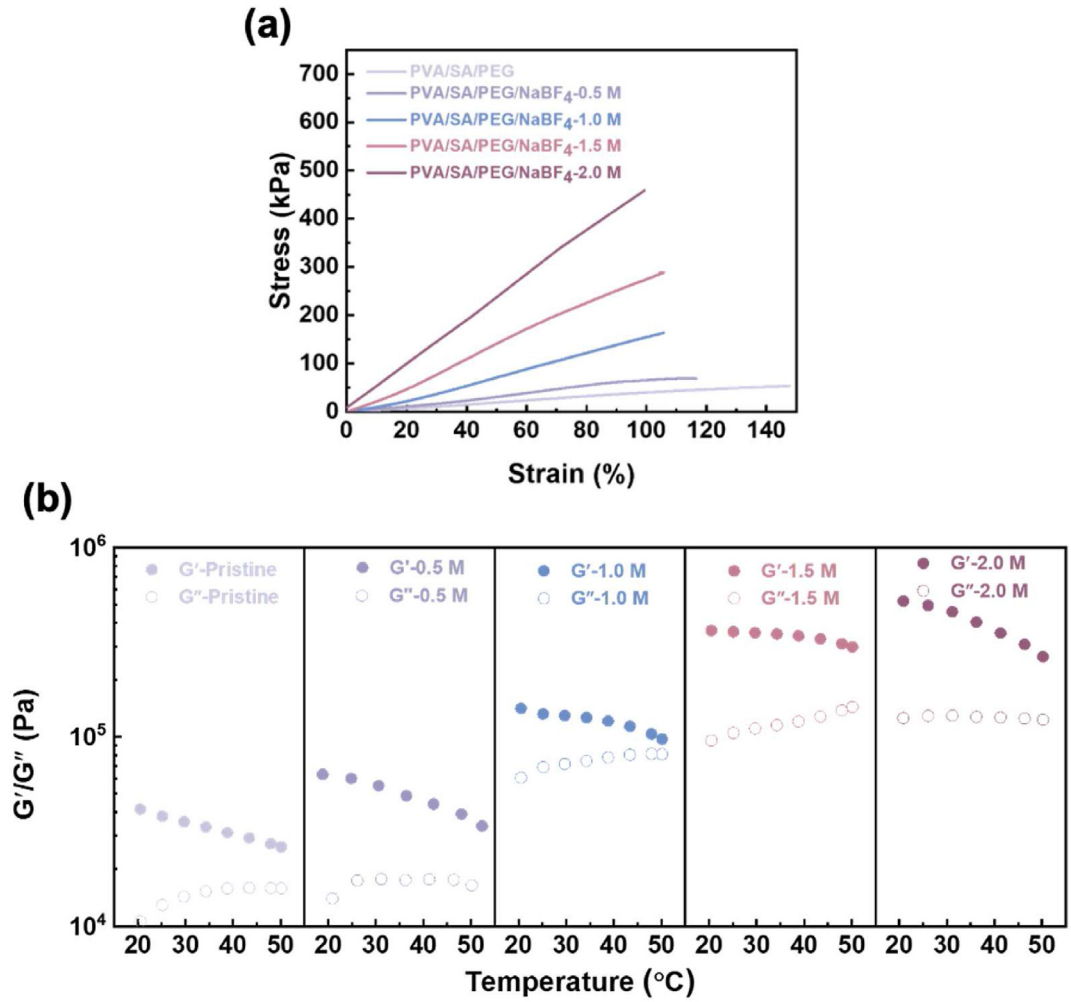

Fig. 4. (a) Tensile stress-strain curve and (b) dynamic mechanical measurement of the storage modulus (G') and loss modulus (G'') of PVA/SA/PEG/$NaBF_4$ hydrogel with varying $NaBF_4$ concentrations.

effect, the ionic Seebeck coefficients can be described using the Onsager transport theory and the Einstein correlation [56]. In a symmetrical electrolyte, the ionic Seebeck coefficient due to thermodiffusion (S_{td}) can be expressed as $S_{td} = \frac{(\hat{S}_+ D_+) - (\hat{S}_- D_-)}{e(D_+ + D_-)}$ where e is the elementary charge, $\hat{S}$ is the Eastman entropy of transfer, D is the mass diffusion coefficient [57], and the subscripts + and − represent the cations and anions, respectively [47]. The Eastman entropy is essentially temperature-dependent and related to the interaction between the solute and the surrounding medium. In the present work, the sign of S_{td} is determined by the difference between the mass diffusion coefficient and values of Na^+ and BF_4^-, while the negatively charged carboxylate groups of SA and the hydroxyl groups of PVA can induce ionic interactions that result in a higher $\hat{S}_+$, which may account for the significant positive thermodiffusion.

To further investigate the PVA/SA/PEG/$NaBF_4$ thermoelectric hydrogel with an ultrahigh ionic Seebeck coefficient, the interplay between Manning's counterion condensation theory and the crystallinity of PVA are considered, as shown in Fig. 5d. According to previous experimental [47,58] and computational analyses [59,60], cations typically have higher mass diffusion coefficient than anions. Manning's counterion condensation theory explains that a small fraction of Na^+ condenses along the negatively-charged SA polymer chain, thus forming coulombic interactions. Meanwhile, the BF_4^- ions experience drags due to the frictional force of the immobilized cations in the vicinity of carboxyl groups. Consequently, those Na^+ cations that do not condense on the SA polymer chain have higher thermal migration rates than the BF_4^- (left-hand side of Fig. 5d) This generates a larger $\hat{S}_+$ and contributes to the achievement of a high ionic Seebeck coefficient. Meanwhile, the presence of crystallinity in the PVA/SA/PEG/$NaBF_4$ hydrogel, as produced by the freeze-thaw method, is probably due to the semicrystalline nature of the PVA. The length of the hydrogen bond in PVA crystals is reported to be within the range of 266–275 p.m. [61,62]. Moreover, Chen et al. [38] have reported that the hydration diameters of H^+ and Cl^- are 564 and 664 p.m., respectively, which are larger than the hydrogen-bond length. In the present work, the larger diameters of the Na^+ and BF_4^- ions compared to those of H^+ and Cl^- ions may make it difficult for these ions to pass through the crystalline regions. However, as ions move from regions with fewer hydrogen bonds (amorphous) to regions with more hydrogen bonds (crystalline), the desolvation of ions may occur [38]. During this desolvation (dehydration) process, the Na^+ ions can easily move into regions of higher crystallity because the Pauling diameter of Na^+ (190 p.m.) [63] is much smaller than the hydrogen-bond length. Therefore, it can be concluded that the ionic Seebeck coefficient is enhanced by an increase in the concentration of mobile Na^+ promoted by the crystallinity of the PVA chains (right-hand

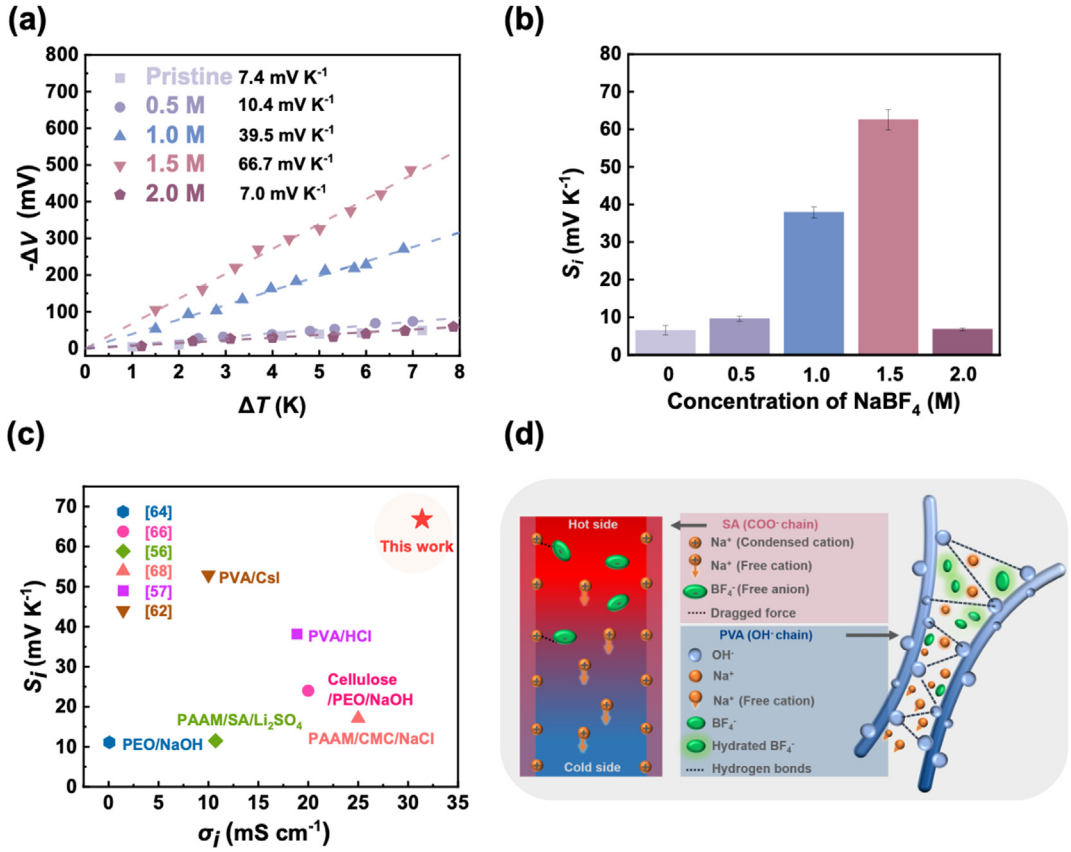

Fig. 5. Thermoelectric properties of PVA/SA/PEG/$NaBF_4$ TCCs. (a) Increase in the -ΔV of the TCCs as a function of Δ*T* between the hot and cold electrodes. (b) Ionic Seebeck coefficient (S_i) of TCCs with varying $NaBF_4$ concentrations. (c) Comparative analysis of the ionic Seebeck coefficient (S_i) versus ionic conductivity (σ_i) curves of the PVA/SA/PEG/$NaBF_4$-1.5 M TCCs in this study and representative TCCs previous reported [34,37,42–44,46]. (d) Schematic illustration depicting interatomic interactions between ions and polymers. On the left hand, a small fraction of Na^+ condenses along the negatively-charged SA polymer chain, thus forming coulombic interactions and the BF_4^- ions drag due to the vicinity of carboxyl groups and Na^+ that do not condense have higher thermal migration rates. On the right hand, during desolvation (dehydration) process, the Na^+ ions can easily migrate into regions with higher crystallinity in the PVA.

side of Fig. 5d). This mechanism is supported by the SEM, FTIR, and XRD results presented in Figs. 2c–f, 3a, and 3b, respectively, where an increase in the $NaBF_4$ concentration indicates improved crystallinity in the PVA. The present results demonstrate that the crystallinity of PVA increases along with the ionic Seebeck coefficient, except when 2.0 M $NaBF_4$ is used (as mentioned above), thereby suggesting that both mechanisms contribute to increasing the difference between the mass diffusion coefficients of Na^+ and BF_4^-, thereby leading to the improvement in the ionic Seebeck coefficient.

The ionic conductivity (σ_i) of a TCC depends on the ionic concentrations (n_i), ionic mobilities (μ_i), and ionic valences (Z_i) of the cations and anions, as expressed by the relationship $\sigma_i = \Sigma n_i e Z_i \mu_i$ [35]. When the TCCs are soaked in high concentrations of $NaBF_4$, the ionic concentration is increased and, hence, the ionic conductivity is increased. Additionally, the presence of a water-rich hydrogel can facilitate the ionic dissociation process, thus resulting in an even higher ionic conductivity. Meanwhile, the ionic mobility in the hydrogel is influenced by the microstructure, which is determined by the double networks formed during the gelation. The ionic conductivities of the pristine PVA/SA/PEG and the PVA/SA/PEG/$NaBF_4$ TCCs with various $NaBF_4$ concentrations are revealed by the electrochemical impedance spectra and bar graph in Fig. 6a and b. Here, the PVA/SA/PEG/$NaBF_4$-2.0 M TCC exhibits a high ionic conductivity (50.79 mS/cm), which is attributed to the soft structure of the PVA, which coordinates with the Na^+ ions and acts as the mobile charge carrier.

The electrochemical performance of the PVA/SA/PEG/$NaBF_4$-1.5 M hydrogel is revealed by the cyclic voltammetry (CV) curve obtained at a scanning rate of 20 mV/s in Fig. S5. The quasi-rectangular shape of this curve indicates that the PVA/SA/PEG/$NaBF_4$-1.5 M hydrogel exhibits the characteristics of a good electric double-layer capacitor. Additionally, the galvanostatic charge and discharge (GCD) curve of the PVA/SA/PEG/$NaBF_4$-1.5 M TCC in Fig. S6 exhibits a nearly symmetrical triangular shape, which indicates typical reversible charge-discharge behavior at the electrolyte-electrode interface.

3.3. Demonstration of ionic thermoelectric supercapacitor (ITESC)

The formation an electrical double layer at the interface between the electrolyte and electrode under the Soret effect holds promise for the development of an ionic thermoelectric supercapacitor (ITESC) for the efficient harvesting of low-grade heat. The operation of an ITESC is demonstrated in Fig. 7, and can be divided into four stages. Thus, in stage I, a Δ*T* of 5 K is applied across the two sides of the hydrogel, thus resulting in the migration of mobile ions from the hot side to the cold side under the Soret effect (Fig. 7a). Because Na^+ has a higher migration rate than BF_4^-, more Na^+ cations accumulate at the cold side, thus generating a voltage gradient (Δ*V*) of −300 mV after 12 min (Fig. 7b). In stage II, when the ITESC is connected to a resistance of 1 kΩ, the charge distribution initiates a spontaneous flow of electrons through the resistance until the charges at the two electrodes are balanced by the electrons and

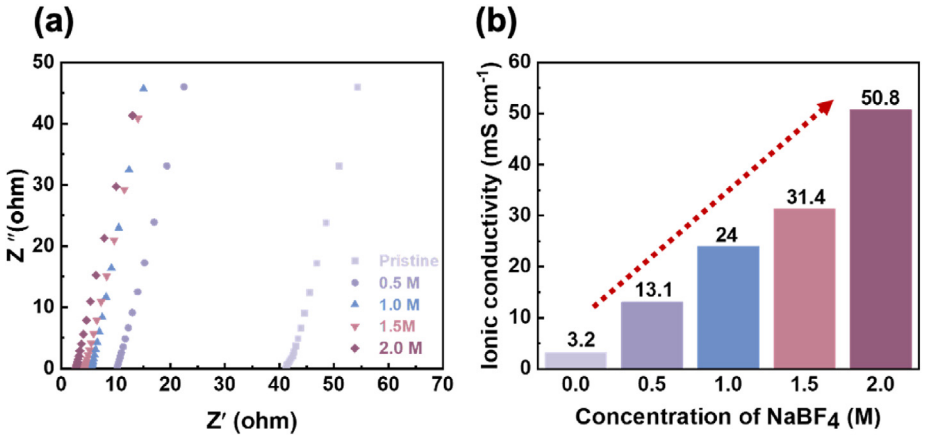

Fig. 6. Ionic conductivity (σ_i) of PVA/SA/PEG/$NaBF_4$ TCCs with varying $NaBF_4$ concentrations. (a) Electrochemical impedance spectroscopy (EIS) spectra. (b) Bar graph depicting the ionic conductivity value.

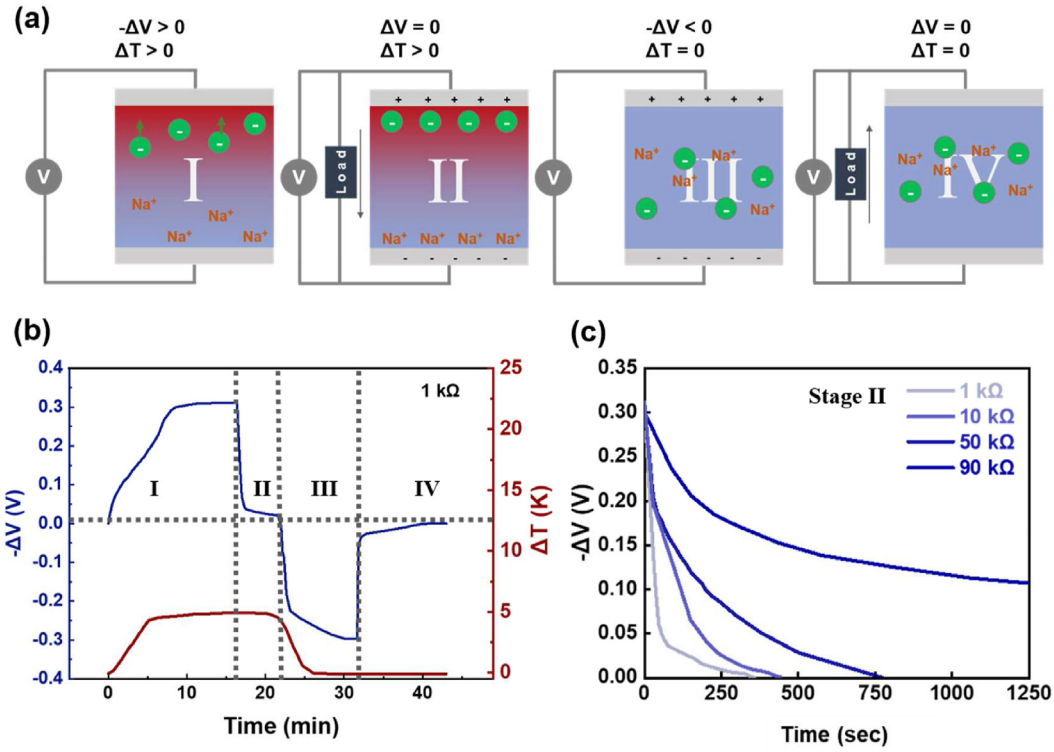

Fig. 7. Performance characterization of PVA/SA/PEG/$NaBF_4$-1.5 M ITESC. (a) Schematic illustration of four stage charging-discharging process of ITESC. (b) Variation in voltage and ΔT throughout the four stage profile, (c) Decay curves of output voltage on external loads with varying resistances connected to the ITESC. The ITESC was evaluated under external loads ranging from 1 to 90 kΩ.

holes from the external circuit, thereby causing the voltage between the two electrodes to decrease to zero. Subsequently, in stage III, upon removal of the heat source and external load, the accumulated ions commence diffusing back to their initial states, while the electrons and holes remain at the two electrodes, thus resulting in a ΔV of approximately 300 mV. Finally, in stage IV, the ITESC is reconnected to the external load, thus prompting the electrons to flow back through the external circuit, and thereby establishing an electron flow in the opposite direction to that observed in stage II. During stage II, the voltage decay rate is seen to diminish from 8 to 64 min as the external resistance is increased from 1 to 90 kΩ, which can be related to the decay time constant (τ), given by $\tau = RC$, where R is the load resistance and C is the capacitance of the TCC, as shown in Fig. 7c. To calculate the harvested energy during different stages which utilize equations such as $E = (\int V\, dt)/R$, where V represents the voltage across the external load and R is the external resistance and dt is the capacitor charging time relating to the resistance of the external load. As the external load resistance increases, more energy is converted during the charging or discharging cycle (Fig. S7). When the resistance of the external load is 90 kΩ, the electricity collected in one thermal cycle is 4 mJ, consisting with previous reports [53,64]. Thus, the thermal cycle experiment illustrated in Fig. 7 successfully demonstrates the potential of the novel PVA/SA/PEG/$NaBF_4$ as ITESC in wearable

thermoelectric devices. Overall, the PVA/SA/PEG/1.5M-$NaBF_4$ hydrogel exhibited a high *PF* of 13.96 mW/m/K^2, a maximum ionic Seebeck coefficient of 66.7 mV/K, and an ionic conductivity of 31.4 mS/cm. These remarkable thermoelectric characteristics were attributed to the synergistic effects of Manning's counterion condensation and enhanced PVA crystallinity, as supported by the SEM, FTIR, and XRD results presented in Figs. 2c–f, 3a, and b, respectively. The hydrogel's unique mechanical properties, including a tensile stress of 69 kPa and a strain of 114%, further contribute to its suitability for wearable device applications. This high performance stretchable ITESC opens up and facilitates subsequent research for achieving self-sustainable electronic devices, including disposable, low-cost, and compact sensors.

4. Conclusion

The present study highlighted the synergistic effects of Manning's counterion condensation induced by sodium alginate (SA) and crystallinity provided by polyvinyl alcohol (PVA) in enhancing the selectivity of ion migration in thermally chargeable capacitors (TCCs). The effects of post-synthetic immersion of the PVA/SA/PEG in various concentrations of tetrafluoroborate ($NaBF_4$) aqueous solution were investigated. The results indicated that the TCCs based the treatment with 1.5 M $NaBF_4$ provide optimal thermoelectric properties, with an ionic Seebeck coefficient of 66.8 mV/K, an ionic conductivity of 31.4 mS/cm, and a power factor of 13.96 mW/m/K^2. This study not only demonstrate the potential of the novel PVA/SA/PEG/$NaBF_4$ as ITESC in wearable thermoelectric devices but also contributing to the advancement of cutting-edge in the field of ionic thermoelectric materials.

CRediT author statement

Yi-Chun Hsiao: Conceptualization, Methodology, Investigation, Visualization, Writing - Original Draft.

Ling-Chieh Lee: Conceptualization, Methodology, Investigation, Visualization, Writing - Original Draft.

Yen-Ting Lin: Conceptualization, Investigation, Validation.

Shao-Huan Hong: Conceptualization, Investigation, Validation.

Kuan-Chieh Wang: Validation.

Shih-Huang Tung: Validation, Writing - Reviewing and Editing.

Cheng-Liang Liu: Conceptualization, Writing- Reviewing and Editing, Supervision, Project administration, Funding acquisition.

Declaration of competing interest

The authors declare the following financial interests/personal relationships which may be considered as potential competing interests: Cheng-Liang Liu reports financial support was provided by National Science and Technology Council. Cheng-Liang Liu reports was provided by Ministry of Education.

Data availability

Data will be made available on request.

Acknowledgment

The authors acknowledge the financial support from 2030 Cross-Generation Young Scholars Program by the National Science and Technology Council (NSTC) in Taiwan under grant 111-2628-E-002-014 and 112-2628-E-002-013 and Academic Research-Career Development Project (Sprout Research Projects) by National Taiwan University (NTU112L7856). This work was also financially supported by the "Advanced Research Center for Green Materials Science and Technology" from The Featured Area Research Center Program within the framework of the Higher Education Sprout Project by the Ministry of Education (112L9006).

Appendix A. Supplementary data

Supplementary data to this article can be found online at https://doi.org/10.1016/j.mtener.2023.101383.

References

[1] F. Brahman, M. Honarmand, S. Jadid, Optimal electrical and thermal energy management of a residential energy hub, integrating demand response and energy storage system, Energy Build. 90 (2015) 65–75. http://10.1016/j.enbuild.2014.12.039.

[2] J. Bao, L. Zhao, A review of working fluid and expander selections for organic rankine cycle, Renew. Sust. Energ. 24 (2013) 325–342. http://10.1016/j.rser.2013.03.040.

[3] P.A. Lolos, E.D. Rogdakis, A kalina power cycle driven by renewable energy sources, Energy 34 (2009) 457–464. http://10.1016/j.energy.2008.12.011.

[4] M. Goodarzi, M. Kiasat, E. Khalilidehkordi, Performance analysis of a modified regenerative brayton and inverse brayton cycle, Energy 72 (2014) 35–43. http://10.1016/j.energy.2014.04.072.

[5] M. Zeng, D. Zavanelli, J. Chen, M. Saeidi-Javash, Y. Du, S. LeBlanc, G.J. Snyder, Y. Zhang, Printing thermoelectric inks toward next-generation energy and thermal devices, Chem. Soc. Rev. 51 (2022) 485–512. http://10.1039/d1cs00490e.

[6] G. Li, Q. An, B. Duan, L. Borgsmiller, M.A. Malki, M. Agne, U. Aydemir, P. Zhai, Q. Zhang, S.I. Morozov, W.A. Goddard, G.J. Snyder, Fracture toughness of thermoelectric materials, Mater. Sci. Eng. R Rep. 144 (2021) 100607. http://10.1016/j.mser.2021.100607.

[7] X.L. Shi, J. Zou, Z.G. Chen, Advanced thermoelectric design: from materials and structures to devices, Chem. Rev. 120 (2020) 7399–7515. http://10.1021/acs.chemrev.0c00026.

[8] Y. Wang, L. Yang, X.L. Shi, X. Shi, L. Chen, M.S. Dargusch, J. Zou, Z.G. Chen, Flexible thermoelectric materials and generators: challenges and innovations, Adv. Mater. 31 (2019) 1807916. http://10.1002/adma.201807916.

[9] H. Wu, X.-l. Shi, J. Duan, Q. Liu, Z.-G. Chen, Advances in Ag_2Se-based thermoelectrics from materials to applications, Energy Environ. Sci. 16 (2023) 1870–1906. http://10.1039/d3ee00378g.

[10] S. Xu, X.-L. Shi, M. Dargusch, C. Di, J. Zou, Z.-G. Chen, Conducting polymer-based flexible thermoelectric materials and devices: from mechanisms to applications, Prog. Mater. Sci. 121 (2021) 100840. http://10.1016/j.pmatsci.2021.100840.

[11] W.-Y. Chen, X.-L. Shi, J. Zou, Z.-G. Chen, Wearable fiber-based thermoelectrics from materials to applications, Nano Energy 81 (2021) 105684. http://10.1016/j.nanoen.2020.105684.

[12] M. Hong, M. Li, Y. Wang, X.L. Shi, Z.G. Chen, Advances in versatile gete thermoelectrics from materials to devices, Adv. Mater. 35 (2023) 2208272. http://10.1002/adma.202208272.

[13] H. Mamur, M.R.A. Bhuiyan, F. Korkmaz, M. Nil, A review on bismuth telluride (bi_2te_3) nanostructure for thermoelectric applications, Renewable Sustainable Energy Rev. 82 (2018) 4159–4169. http://10.1016/j.rser.2017.10.112.

[14] G. Tan, F. Shi, S. Hao, H. Chi, L.D. Zhao, C. Uher, C. Wolverton, V.P. Dravid, M.G. Kanatzidis, Codoping in snte: enhancement of thermoelectric performance through synergy of resonance levels and band convergence, J. Am. Chem. Soc. 137 (2015) 5100–5112. http://10.1021/jacs.5b00837.

[15] Q. Yan, M.G. Kanatzidis, High-performance thermoelectrics and challenges for practical devices, Nat. Mater. 21 (2022) 503–513. http://10.1038/s41563-021-01109-w.

[16] Z.H. Zheng, D.L. Zhang, J.Y. Niu, X.L. Shi, T.B. Chen, Y.F. Chen, F. Li, G.X. Liang, Y.X. Chen, P. Fan, Z.G. Chen, Achieving ultrahigh power factor in n-type Ag2Se thin films by carrier engineering, Mater, Today Energy 24 (2022). http://ARTN100933310.1016/j.mtener.2021.100933.

[17] S. Sun, X.L. Shi, M. Li, T. Wu, L. Yin, D. Wang, Q. Liu, Z.G. Chen, Ultrafast and cost-effective fabrication of high-performance carbon-based flexible thermoelectric hybrid films and their devices, ACS Appl. Mater. Interfaces 15 (2023) 25650–25660. http://10.1021/acsami.3c05226.

[18] X.L. Shi, W.D. Liu, M. Li, Q. Sun, S.D. Xu, D. Du, J. Zou, Z.G. Chen, A solvothermal synthetic environmental design for high-performance SnSe-based thermoelectric materials, Adv. Energy Mater. 12 (2022). http://10.1002/aenm.202200670.

[19] X. Mu, X.-L. Shi, J. Zhou, H. Chen, T. Yang, Y. Wang, L. Miao, Z.-G. Chen, Self-hygroscopic and smart color-changing hydrogels as coolers for improving energy conversion efficiency of electronics, Nano Energy 108 (2023). http://10.1016/j.nanoen.2023.108177.

[20] M. Bonetti, S. Nakamae, M. Roger, P. Guenoun, Huge seebeck coefficients in nonaqueous electrolytes, J. Chem. Phys. 134 (2021) 114513. http://10.1063/1.3561735.

[21] H. Cheng, Q. Le, Z. Liu, Q. Qian, Y. Zhao, J. Ouyang, Ionic thermoelectrics: principles, materials and applications, J. Mater. Chem. C 10 (2022) 433–450. http://10.1039/d1tc05242j.
[22] Z. Lei, P. Wu, Bioinspired quasi-solid ionic conductors: materials, processing, and applications, Acc. Mater. Res. 2 (2021) 1203–1214. http://10.1021/accountsmr.1c00165.
[23] M. Li, M. Hong, M. Dargusch, J. Zou, Z.-G. Chen, High-efficiency thermocells driven by thermo-electrochemical processes, Trends in Chemistry 3 (2021) 561–574. http://10.1016/j.trechm.2020.11.001.
[24] H. Wu, Y. Huang, F. Xu, Y. Duan, Z. Yin, Energy harvesters for wearable and stretchable electronics: from flexibility to stretchability, Adv. Mater. 28 (2016) 9881–9919. http://10.1002/adma.201602251.
[25] Y. Liu, H. Wang, P.C. Sherrell, L. Liu, Y. Wang, J. Chen, Potentially wearable thermo-electrochemical cells for body heat harvesting: from mechanism, materials, strategies to applications, Adv. Sci. 8 (2021) 2100669. http://10.1002/advs.202100669.
[26] N. Pataki, P. Rossi, M. Caironi, Solution processed organic thermoelectric generators as energy harvesters for the internet of things, Appl. Phys. Lett. 121 (2022) 230501. http://10.1063/5.0129861.
[27] S. Sun, M. Li, X.L. Shi, Z.G. Chen, Advances in ionic thermoelectrics: from materials to devices, Adv. Energy Mater. 13 (2023) 2203692. http://10.1002/aenm.202203692.
[28] X. Wu, N. Gao, H. Jia, Y. Wang, Thermoelectric converters based on ionic conductors, Chem. Asian J. 16 (2021) 129–141. http://10.1002/asia.202001331.
[29] D. Zhao, A. Würger, X. Crispin, Ionic thermoelectric materials and devices, J. Energy Chem. 61 (2021) 88–103. http://10.1016/j.jechem.2021.02.022.
[30] Y.H. Gang Li, Jihao Chen, Lirong Liang, Zhuoxin Liu, Fu Jia, Chunyu Du, Guangming Chen, Thermoelectric and photoelectric dual modulated sensors for human internet of things application in accurate fire recognition and warning, Adv. Funct. Mater. (2023), https://doi.org/10.1002/adfm.202303861.
[31] M.C. Chunyu Du, Gang Li, Yue Hu, Yichuan Zhang, Lirong Liang, Zhuoxin Liu, Guangming Chen, Toward precision recognition of complex hand motions: wearable thermoelectrics by synergistic 2d nanostructure confinement and controlled reduction, Adv. Funct. Mater. 202206083 (2022), https://doi.org/10.1002/adfm.202206083.
[32] H. Lv, L. Liang, Y. Zhang, L. Deng, Z. Chen, Z. Liu, H. Wang, G. Chen, A flexible spring-shaped architecture with optimized thermal design for wearable thermoelectric energy harvesting, Nano Energy 88 (2021). http://10.1016/j.nanoen.2021.106260.
[33] J. Duan, G. Feng, B. Yu, J. Li, M. Chen, P. Yang, J. Feng, K. Liu, J. Zhou, Aqueous thermogalvanic cells with a high seebeck coefficient for low-grade heat harvest, Nat. Commun. 9 (2018) 5146. http://10.1038/s41467-018-07625-9.
[34] D. Zhao, H. Wang, Z.U. Khan, J.C. Chen, R. Gabrielsson, M.P. Jonsson, M. Berggren, X. Crispin, Ionic thermoelectric supercapacitors, Energy Environ. Sci. 9 (2016) 1450–1457. http://10.1039/c6ee00121a.
[35] H. Cheng, J. Ouyang, Soret effect of ionic liquid gels for thermoelectric conversion, J. Phys. Chem. Lett. 13 (2022) 10830–10842. http://10.1021/acs.jpclett.2c02645.
[36] C. Chi, M. An, X. Qi, Y. Li, R. Zhang, G. Liu, C. Lin, H. Huang, H. Dang, B. Demir, Y. Wang, W. Ma, B. Huang, X. Zhang, Selectively tuning ionic thermopower in all-solid-state flexible polymer composites for thermal sensing, Nat. Commun. 13 (2022) 221. http://10.1038/s41467-021-27885-2.
[37] J. Chen, L. Zhang, Y. Tu, Q. Zhang, F. Peng, W. Zeng, M. Zhang, X. Tao, Wearable self-powered human motion sensors based on highly stretchable quasi-solid state hydrogel, Nano Energy 88 (2021) 106272. http://10.1016/j.nanoen.2021.106272.
[38] Q. Chen, B. Chen, S. Xiao, J. Feng, J. Yang, Q. Yue, X. Zhang, T. Wang, Giant thermopower of hydrogen ion enhanced by a strong hydrogen bond system, ACS Appl. Mater. Interfaces 14 (2022) 19304–19314. http://10.1021/acsami.1c24698.
[39] H. Cheng, X. He, Z. Fan, J. Ouyang, Flexible quasi-solid state ionogels with remarkable seebeck coefficient and high thermoelectric properties, Adv. Energy Mater. 9 (2019) 1901085. http://10.1002/aenm.201901085.
[40] C.G. Han, X. Qian, Q. Li, B. Deng, Y. Zhu, Z. Han, W. Zhang, W. Wang, S.P. Feng, G. Chen, W. Liu, Giant thermopower of ionic gelatin near room temperature, Science 368 (2020) 1091–1098. http://10.1126/science.aaz5045.
[41] X. He, H. Cheng, S. Yue, J. Ouyang, Quasi-solid state nanoparticle/(ionic liquid) gels with significantly high ionic thermoelectric properties, J. Mater. Chem. A 8 (2020) 10813–10821. http://10.1039/d0ta04100a.
[42] Y. He, Q. Zhang, H. Cheng, Y. Liu, Y. Shu, Y. Geng, Y. Zheng, B. Qin, Y. Zhou, S. Chen, J. Li, M. Li, G.O. Odunmbaku, C. Li, T. Shumilova, J. Ouyang, K. Sun, Role of ions in hydrogels with an ionic seebeck coefficient of 52.9 mv k^{-1}, J. Phys. Chem. Lett. 13 (2022) 4621–4627. http://10.1021/acs.jpclett.2c00845.
[43] F. Jiao, A. Naderi, D. Zhao, J. Schlueter, M. Shahi, J. Sundström, H. Granberg, J. Edberg, U. Ail, J. Brill, T. Lindström, M. Berggren, X. Crispin, Ionic thermoelectric paper, J. Mater. Chem. A 5 (2017) 16883–16888. http://10.1039/c7ta03196c.
[44] T. Li, X. Zhang, S.D. Lacey, R. Mi, X. Zhao, F. Jiang, J. Song, Z. Liu, G. Chen, J. Dai, Y. Yao, S. Das, R. Yang, R.M. Briber, L. Hu, Cellulose ionic conductors with high differential thermal voltage for low-grade heat harvesting, Nat. Mater. 18 (2019) 608–613. http://10.1038/s41563-019-0315-6.
[45] C. Liu, Q. Li, S. Wang, W. Liu, N.X. Fang, S.-P. Feng, Ion regulation in double-network hydrogel module with ultrahigh thermopower for low-grade heat harvesting, Nano Energy 92 (2022) 106738. http://10.1016/j.nanoen.2021.106738.
[46] X. Yang, Y. Tian, B. Wu, W. Jia, C. Hou, Q. Zhang, Y. Li, H. Wang, High-performance ionic thermoelectric supercapacitor for integrated energy conversion-storage, Energy Environ. Mater. 5 (2021) 954–961. http://10.1002/eem2.12220.
[47] B. Chen, Q. Chen, S. Xiao, J. Feng, X. Zhang, T. Wang, Giant negative thermopower of ionic hydrogel by synergistic coordination and hydration interactions, Sci. Adv. 7 (2021) eabi7233, http://10.1126/sciadv.abi7233.
[48] J. Kamcev, D.R. Paul, B.D. Freeman, Ion activity coefficients in ion exchange polymers: applicability of Manning's counterion condensation theory, Macromolecules 48 (2015) 8011–8024. http://10.1021/acs.macromol.5b01654.
[49] O. Hu, J. Lu, G. Chen, K. Chen, J. Gu, S. Weng, L. Hou, X. Zhang, X. Jiang, An antifreezing, tough, rehydratable, and thermoplastic poly(vinyl alcohol)/sodium alginate/poly(ethylene glycol) organohydrogel electrolyte for flexible supercapacitors, ACS Sustain. Chem. Eng. 9 (2021) 9833–9845. http://10.1021/acssuschemeng.1c02464.
[50] H. Adelnia, R. Ensandoost, S. Shebbrin Moonshi, J.N. Gavgani, E.I. Vasafi, H.T. Ta, Freeze/thawed polyvinyl alcohol hydrogels: present, past and future, Eur. Polym. J. 164 (2022) 110974. http://10.1016/j.eurpolymj.2021.110974.
[51] C. Cao, Y. Li, Highly stretchable calcium ion/polyacrylic acid hydrogel prepared by freezing–thawing, J. Mater. Sci. 55 (2020) 5340–5348. http://10.1007/s10853-019-04332-8.
[52] E. Park, J.H. Ryu, D. Lee, H. Lee, Freeze-thawing-induced macroporous catechol hydrogels with shape recovery and sponge-like properties, ACS Biomater. Sci. Eng. 7 (2021) 4318–4329. http://10.1021/acsbiomaterials.0c01767.
[53] G. Fan, K. Liu, H. Su, Y. Luo, Y. Geng, L. Chen, B. Wang, Z. Mao, X. Sui, X. Feng, Mesoscopic confined ionic thermoelectric materials with excellent ionic conductivity for waste heat harvesting, Chem. Eng. J. 434 (2022). http://10.1016/j.cej.2022.134702.
[54] S. Mardi, D. Zhao, K. Tybrandt, A. Reale, X. Crispin, Interfacial effect boosts the performance of all-polymer ionic thermoelectric supercapacitors, Adv. Mater. Interfac. 9 (2022) 2201058. http://10.1002/admi.202201058.
[55] A.I. Van Den Bulcke, B. Bogdanov, N. De Rooze, E.H. Schacht, M. Cornelissen, H. Berghmans, Structural and rheological properties of methacrylamide modified gelatin hydrogels, Biomacromolecules 1 (2000) 31–38. http://10.1021/bm990017d.
[56] J.C. Goodrich, F.M. Goyan, E.E. Morse, R.G. Preston, M.B. Young, Applications of the eastman thermocell equation.[1] i. Certain absolute ionic entropies and entropies of transfer of alkali metal and tetraalkylammonium bromides and hydroxides, J. Am. Chem. Soc. 72 (2002) 4411–4418. http://10.1021/ja01166a020.
[57] W. Köhler, B. Müller, Soret and mass diffusion coefficients of toluene/n-hexane mixtures, J. Chem. Phys. 103 (1995) 4367–4370. http://10.1063/1.470677.
[58] R. Konefal, Z. Moravkova, B. Paruzel, V. Patsula, S. Abbrent, K. Szutkowski, S. Jurga, Effect of pamam dendrimers on interactions and transport of litfsi and natfsi in propylene carbonate-based electrolytes, Polymers 12 (2020) 1595. http://10.3390/polym12071595.
[59] D. Aryal, V. Ganesan, Reversal of salt concentration dependencies of salt and water diffusivities in polymer electrolyte membranes, ACS Macro Lett. 7 (2018) 739–744. http://10.1021/acsmacrolett.8b00333.
[60] D. Aryal, V. Ganesan, Impact of cross-linking of polymers on transport of salt and water in polyelectrolyte membranes: a mesoscopic simulation study, J. Chem. Phys. 149 (2018) 224902. http://10.1063/1.5057708.
[61] W. Fuller, Hydrogen bond lengths and angles observed in crystals, J. Chem. Phys. 63 (2002) 1705–1717. http://10.1021/j150580a035.
[62] G.I. Taylor, The spectrum of turbulence, Proc. Math. Phys. Eng. Sci. 164 (1997) 476–490. http://10.1098/rspa.1938.0032.
[63] A. Villard, O. Bernard, J.-F. Dufrêche, Non-additivity of ionic radii in electrolyte solutions: hofmeister effect on mixtures modeled by an associated msa model, J. Mol. Liq. 270 (2018) 30–39. http://10.1016/j.molliq.2018.01.125.
[64] Z. Liu, H. Cheng, Q. Le, R. Chen, J. Li, J. Ouyang, Giant thermoelectric properties of ionogels with cationic doping, Adv. Energy Mater. 12 (2022). http://10.1002/aenm.202200858.